Accepted Manuscript

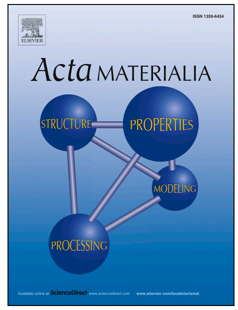

Grain Boundary Segregation and Intermetallic Precipitation in Coarsening Resistant Nanocrystalline Aluminum Alloys

A. Devaraj, W. Wang, R. Vemuri, L. Kovarik, X. Jiang, M. Bowden, J.R. Trelewicz, S. Mathaudhu, A. Rohatgi

PII: S1359-6454(18)30750-X

DOI: 10.1016/j.actamat.2018.09.038

Reference: AM 14847

To appear in: *Acta Materialia*

Received Date: 2 June 2018

Revised Date: 20 August 2018

Accepted Date: 18 September 2018

Please cite this article as: A. Devaraj, W. Wang, R. Vemuri, L. Kovarik, X. Jiang, M. Bowden, J.R. Trelewicz, S. Mathaudhu, A. Rohatgi, Grain Boundary Segregation and Intermetallic Precipitation in Coarsening Resistant Nanocrystalline Aluminum Alloys, *Acta Materialia* (2018), doi: https://doi.org/10.1016/j.actamat.2018.09.038.

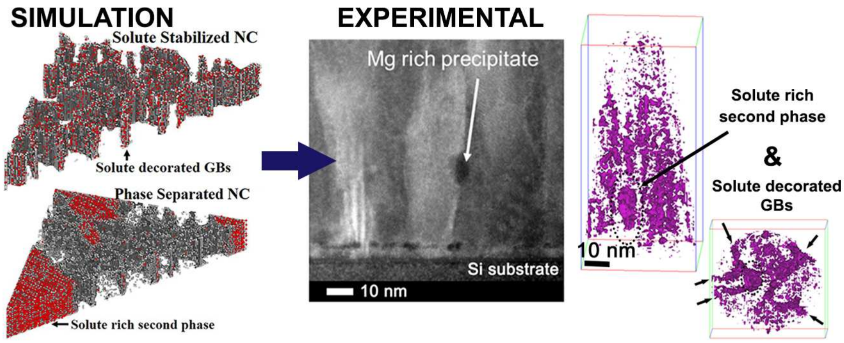
SIMULATION
Solute Stabilized NC
Solute decorated GBs
Phase Separated NC
Solute rich second phase
EXPERIMENTAL
Mg rich precipitate
Si substrate
10 nm
Solute rich
second phase
&
Solute decorated
GBs
10 nm

Grain Boundary Segregation and Intermetallic Precipitation in Coarsening Resistant Nanocrystalline Aluminum Alloys

A. Devaraj[1,*], W. Wang[2], R. Vemuri[4], L. Kovarik[4], X. Jiang[5], M. Bowden[4], J.R. Trelewicz[2,3], S. Mathaudhu[5, 6], A. Rohatgi[5,*]

[1]Physical and Computational Sciences Directorate, Pacific Northwest National Laboratory

[2]Department of Materials Science and Chemical Engineering, Stony Brook University

[3]Institute for Advanced Computational Science, Stony Brook University

[4]Environmental Molecular Sciences Laboratory, Pacific Northwest National Laboratory

[5]Energy and Environmental Directorate, Pacific Northwest National Laboratory

[6]Mechanical Engineering and Materials Science and Engineering, University of California, Riverside

Corresponding authors: arun.devaraj@pnnl.gov; Aashish.rohatgi@pnnl.gov

Abstract

In-spite of all of the unique properties of nanocrystalline materials, they are notorious when it comes to their susceptibility to thermally induced grain coarsening, thus imposing an upper limit to their application temperature. In this study, we demonstrate a coupled Monte Carlo-molecular dynamics simulation-guided experimental approach of improving the resistance to thermally induced grain coarsening in light-weight nanocrystalline Al-Mg alloys. The structure, grain boundary segregation of Mg, and extent of grain coarsening of the Al-Mg alloys were characterized using plan view and cross-sectional transmission electron microscopy and atom probe tomography. Coarsening resistance is attributed to a combination of thermodynamic stabilization of grain boundaries by controlled Mg segregation, and kinetic stabilization through pinning of the boundaries with nanoscale intermetallic precipitates. Thus, we highlight the opportunities in extending the upper limit of application temperature for nanocrystalline alloys by using a complementary thermodynamic and kinetic stabilization approach.

Keywords: Al-Mg, grain boundary segregation, intermetallic precipitation, nanocrystalline, stability

1. Introduction

In-spite of many unique mechanical properties demonstrated by nanostructured alloys, exposure of such alloys to high temperatures during synthesis or during use can induce drastic grain coarsening, rendering them no longer usable in their intended applications [1-3]. This problem of poor resistance to grain coarsening in nanocrystalline materials arises from the large proportion of atoms being situated along the grain boundaries with higher excess free energy than the atoms in the interior of grains [1]. Hence there exists a large driving force for reduction in grain boundary area (by grain-growth) so as to reduce the excess free energy of the system. To increase the stability of nanocrystalline alloys during thermal annealing, this large driving force needs to be dealt with either by reducing the free energy of grain boundaries (e.g. by solute segregation) or by kinetic pinning of grain boundary motion [4-6]. Thermodynamic stabilization approaches, sometimes in conjunction with kinetic stabilization approaches, have also been used in several high density alloy systems such as W-Ti [7], Ni-W [8, 9], Fe-Cr-Zr [10], Fe-Cr-Hf [11], Fe-Zr [12], Fe-Ni-Zr [13], Cu-Ta [14, 15], Fe-Mg [16] etc. In such studies, concurrent or competing phenomena of grain boundary solute segregation and precipitation of phases such as oxides, carbides or intermetallics, have been shown to be responsible for increasing the resistance to grain coarsening. However especially when it comes to light weight alloys, at present we do not have a predictive control of such concurrent mechanisms responsible for enhancing the grain coarsening resistance of alloys. This lack of understanding is even more pronounced when it comes to alloys with a driving force for simultaneous solute segregation to grain boundaries and intermetallic precipitation as is the case of Al-Mg alloys.

For curvature-driven grain-growth, the velocity, v, of a grain boundary can be written as[17]

$$v = M \times P = M_0 \exp[-Q_m/RT]\, 2\gamma_b/r \quad (1)$$

where M is the mobility and the kinetic parameter, while P is the driving force (or pressure) and the thermodynamic parameter. In Eq. 1, M_0 is the pre-exponential term, Q_m is the activation energy for grain boundary mobility, R is the ideal gas constant, T is the absolute temperature, γ_b is the interfacial energy per unit area and r is the radius of the grain. The proposed thermodynamic approach for improving thermal stability of the nanostructures corresponds to strategies that reduce the pressure term (i.e. $P = 2\gamma_b/r$) in Eq. 1 which essentially focus on reducing the interfacial energy (γ_b) whose temperature dependency is minimal[10, 17]. However, competing and concurrent effect of solute drag, and formation of nano-sized precipitates that can pin grain boundaries against motion may also contribute to thermal stability via kinetic stabilization[1]. The efficiency of precipitates in pinning the grain boundaries, as defined by Zener pinning is $P = \frac{3F\gamma}{2d}$ where P is the pressure exerted by the precipitates on unit area of grain boundary, F is volume fraction of particles with size d which are assumed to be spherical and randomly distributed in the alloy and γ is the grain boundary energy[18].

While the mechanisms of thermodynamic and kinetic stabilization are generally known within the scientific community, their interplay is becoming increasingly more important as new nanocrystalline materials containing grain boundary phases [19, 20] and nanoscale precipitates [20] are being realized. The Al-Mg system provides an opportunity to consider complementary stabilization mechanisms due to their propensity for grain boundary segregation [21-25] and the potential to form Al_3Mg_2 precipitates [26]. Past studies of nanostructured Al-Mg have typically relied on severe plastic deformation (SPD) based techniques (e.g. ball-milling, equal-channel angular processing (ECAP), high-pressure torsion (HPT), etc.) to create the starting nanostructure. [27-39]. On annealing such deformation-processed Al-Mg alloys with high levels of stored energy, recovery and recrystallization events were often observed, providing either a coarse grain structure or bimodal grain size distribution with or without second phase precipitates of Al_3Mg_2[35]. SPD processing is expected to produce non-equilibrium grain boundaries with excess density of dislocations which in turn are expected to be the pinning sites for Mg causing increased Mg segregation at grain boundaries [40, 41]. Prior research on Al-Mg alloys is summarized in Table 1 and shows that there are disagreements in the literature, where some studies reported the formation of super-saturated solid solution of Mg in Al, while others reported the formation of non-equilibrium grain boundaries with grain boundary depletion or segregation of Mg or formation of Al_3Mg_2 precipitates [30, 34, 38, 40, 42-44]. The thermal stability of nanostructured Al-Mg systems was not evaluated in sufficient detail in past either, predominantly limited by spatial resolution and sensitivity of analysis methods to verify the existence (or absence) of thermodynamic or kinetic stabilization mechanisms. Within the limited past work reported on thermal stability of nanocrystalline Al-Mg alloys, significant variation is also observed i.e. some studies reported grain growth upon annealing (e.g. 200 nm → 10 microns [39] and 100 nm → 10 micron [36]) whether Mg was present in solid solution [36, 39] or in both solid solution and precipitates [37]. Therefore, the present work was undertaken to systematically investigate thermal stabilization in nanocrystalline Al-Mg alloys through a computationally-guided experimental approach while avoiding or eliminating any influence of prior deformation during processing.

Table 1: Summary of literature on nanostructured Al-Mg binary alloys, sorted in the order of increasing Mg%. The literature reported wt % value is listed in normal font while the corresponding converted at % value is italicized.

Reference	Mg Wt.% (At.%)	Fabrication method	Analyzed by	Average Grain size	Mg distribution	Evaluation of Thermal stability
M. P. Liu et.al. 2010[33]	0.5 (*0.55%*), 1% (*1.1%*), 2.5% (*2.8%*)	Cast-homogenized+ HPT	TEM, XRD	Grain size reduced from 120-55nm for 0.5-2.5 wt% Mg	Supersaturated solid solution with equilibrium and non-equilibrium grain boundaries	Not studied
J. Wang et. al. 1996[39]	3% (3.32 %)	ECAP and post annealing	TEM, DSC	~200nm	Supersaturated solid solution	On annealing up to 300 °C, grain size grows to 10 µm.
M. Furukawa et.al. 1996 [36]	3% (3.32%)	ECAP, torsion strained, post annealed	TEM	90nm and higher	Super saturated solid solution	Grains grew from 100nm to 10-15 µm range on annealing up to 300 °C. On further higher temperature annealing grain size grew to 100 µm range.
R. Hayes et.al. 1999[31]	4% (4.42 %)	Cryomilling+HIP	TEM-SAED, XRD	~300nm	Al3Mg2 and Al-O and Al-N precipitates inside the grain interiors and grain boundaries	Creep tested at 300 °C, precipitates suggested to play role in pinning grain boundary (GB) sliding
K. M. Youssef et.al. 2006[28]	4.5% (5%)	Mechanical alloying at room temperature and 77K	SEM, TEM, XRD	26nm	Supersaturated solid solution.	Not studied
B. B. Straumal	5% (5.5%),	HPT	TEM-EDS,	~150nm for Al-5%	Supersaturated solid solution	Not studied

et.al. 2004 [30]	10% (11%)		SAED, XRD	Mg and ~90nm for Al-10% Mg)	with <10nm sized Al_3Mg_2 precipitates	
F. Zhou et. al. 2003 [35]	6.4% (7%)	Cryomilled	DSC, XRD, TEM	~ 25nm	Supersaturated solid solution	On annealing to 370 °C, recovery observed from 100-230 °C and recrystallization observed up to 370 °C leading to generation of bimodal grain sizes.
F. Zhou et. al. 2002 [29]	7.5% (8.3%)	Cryomilling	XRD, SEM	~20nm	Supersaturated solid solution	Al-7.5% Mg reported to be thermally stable.
Y. S. Park et.al. 2004[27]	7.5% (8.3%)	Cryomilling and HIP, extrusion	SEM, TEM	Bimodal: mix of Coarse (1-4 µm) grains and nanocrystals (114-197 nm)	Supersaturated solid solution.	Not studied
B. Q. Han et. al. 2005 [37]	7.5% (8.26%)	Cryomilled and extruded	TEM, XRD	~260nm	Supersaturated solid solution with second phase oxide or Al-Mg intermettalic precipitates	500°C annealing lead to some grains to grow to 550 nm.
G. J. Fan et al. 2006[32]	7.5% (8.26%)	Mixture of coarse grained powder and Cryomilled powder + HIP and Extrusion	OM, SEM, TEM, XRD	Bimodal grain size: coarse grains (2.7-3.5 µm) in a matrix of fine grains (120-338nm)	Supersaturated FCC Al(Mg) solid solution	Not studied

R. Goswami et. al. 2014 [34]	7.5 % (8.26%)	Cryomilled + consolidated and extrude + aged at 175°C for 10 days	TEM-EDS and XRD	50-300nm	Supersaturated solid solution with Al3Mg2 precipitation and some grain boundaries enriched in Mg (based on STEM-EDS)	Ageing at 175° for 10 days led to precipitation of Al_3Mg_2
S. C. Pun et. al. [21]	6.35% (7 %)	Mechanically milled + annealed at 200°C for 1 hr	TEM-EDS, SAED, XRD	24 nm (measured by XRD)	Mg shown to be segregated to grain boundaries using TEM-EDS	Not studied.

Acronyms:
DSC: Differential scanning calorimetry
ECAP: Equi-channel angular pressing
EDS: Energy dispersive spectroscopy
HIP: Hot iso-static pressing
OM: Optical microscopy
SAED:Selected Area Electron Diffraction
SEM: Scanning electron microscopy
TEM: Transmission electron microscopy
STEM: Scanning Transmission Electron Microscopy
XRD: X-ray diffraction

In this work we used a computationally-guided experimental approach to design coarsening resistant nanocrystalline Al-Mg binary alloys. A hybrid Monte Carlo (MC)/molecular dynamics (MD) model was used to explore thermodynamically preferred states in nanocrystalline Al-Mg alloys with a focus on solute distribution and its implications for nanostructure stability. In particular, we predict the concentration of Mg solute segregated to grain boundaries for alloys of Al-5 and Al-10 at. % Mg at temperatures of 25 and 300 °C. Guided by the simulation predictions, corresponding Al-Mg thin films were deposited through magnetron co-sputtering of Al and Mg and the films were characterized by transmission electron microscopy (TEM) and atom probe tomography (APT) to characterize nanoscale structural features and their dependence on the solute distribution. The films were annealed at 300^{o}C for 3 hours to analyze their coarsening resistance. Model predictions are used to understand grain boundary segregation and its role in precipitation in the experimental materials, thus identifying a critical mechanism that can enable synergistic effects between thermodynamic stabilization via grain boundary (GB) segregation and kinetic pinning through nanoscale precipitation along grain boundaries in nanostructured alloys.

2. Methods and Materials

2.1 Computational Methods

Atomistic simulations employed columnar nanocrystalline structures designed to emulate the experimental materials while providing a combination of exceptional computational efficiency and the ability to capture 3D grain growth dynamics[45]. A planar Voronoi tessellation method[46] was used to produce 2D polycrystal templates containing 50 grains with an average grain size of 5 nm. A total of 5 structures were selected from 50 individual tessellations and specifically chosen based on the absence of unstable polygons with a very small number of sides. These 2D templates were used to produce <001> textured columnar nanocrystalline structures containing <001> tilt boundaries with a distribution of misorientation angles. The thickness of the simulation cell was assigned based on the minimum number of atoms required for the hybrid Monte Carlo (MC)-molecular dynamics (MD) scheme, which is described in the work of Sadigh, et al.[47] Given the number of grains and an average grain size of 5 nm, the total size of the simulation cell was 31.5 x 31.5 x 6 nm and contained approximately 362,000 atoms. The embedded-atom method (EAM) potential developed by Mendelev et al.[48] for Al-Mg was used with an isobaric– isothermal (NPT) thermostat and a time-step of 2 fs.

Simulations were conducted using the Large-scale Atomic/Molecular Massively Parallel Simulator (LAMMPS) platform[49]. Starting with the pure Al structure, Mg atoms were added through random site replacement to produce alloy compositions of Al-5 and Al-10 at. % Mg. Energy-minimized structures were then achieved using a conjugate gradient (CG) relaxation to a final relative energy convergence of 10^{-12} followed by a MD relaxation for 0.2 ns. To explore solute redistribution through simulated annealing, the structures were evolved for 10 ns at temperatures of 25 and 300 °C using the hybrid MC/MD technique. The Ovito package[50] was used for visualization and quantification of distributions with grains distinguished using the common neighbor analysis (CNA) method,[51] which indexes each atom according to its local atomic coordination. The grain boundary solute excess, Γ, was calculated following the Gibbsian interfacial excess [52] defined by:

$$\Gamma = \frac{1}{A_{gb}}\left(N_{gb}^{Mg} - N_{c}^{Mg}\left(\frac{N_{gb}^{Al}}{N_{c}^{Al}}\right)\right) \tag{1}$$

where A_{gb} represents the grain boundary area and N the number of Mg or Al atoms in the grain boundary or grain interior denoted by the subscripts 'gb' and 'c', respectively. In instances where precipitation was detected, solute and solvent atoms in the precipitated phase were excluded from the solute excess calculation.

2.2 Experimental Materials and Methods

High-purity nanocrystalline thin films of pure Al, and Al-Mg alloy with nominal compositions of Al-5 at % (4.5 wt.%) Mg (henceforth, Al-5% Mg) and Al-10 at % (9 wt.%) Mg (henceforth, Al-10% Mg), were fabricated using magnetron sputtering (Denton Vacuum). Al and Al-Mg films of thickness 100 nm were deposited on low-stress SiN (30 nm thick) TEM windows (for TEM/STEM analysis) and on doped Si microtip array specimen posts (for atom probe tomography (APT)). The TEM windows and the microtip arrays were clamped on a copper support plate which, in turn, was clamped on a water-cooled substrate holder. The sputtered film thickness and the deposition rate were simultaneously monitored using a quartz crystal thickness monitor. Al deposition for all films was performed using ~130 W DC sputtering power and Mg was deposited using ~12 W RF sputtering power, with minor variations to incorporate different compositions. The deposition power was adjusted for both materials to maintain deposition rates of 2.8 Å/s for Al for all samples, 0.2 Å/s for Mg for Al-5% Mg and 0.5 Å/s for Mg for Al-10% Mg. A base pressure of at least $5x10^{-7}$ torr was achieved in the chamber before starting a deposition run and an ultra-high-purity argon with a pressure of 2.2 mtorr was used at a flow rate of 40 sccm (standard cubic centimeter per minute) during sputtering. The thickness of the sputtered films was measured using cross-sectional TEM imaging. Thermal stability of the Al and Al-Mg films, sputtered on the TEM grid, was studied by annealing them at 300 °C for 3 hours within the vacuum chamber itself at the end of the sputtering run and without any exposure to atmosphere (at $5x10^{-7}$ torr vacuum). At the end of 3 hours annealing, the samples were cooled down to room-temperature with the high vacuum being maintained during the entire heat-treatment duration to avoid any potential oxidation of the films at elevated temperatures. Upon cooling, the annealed samples were removed from the vacuum chamber and analyzed in TEM for grain growth and Mg distribution in the matrix.

Scanning transmission electron microscopy (S/TEM) observations were acquired using an aberration corrected FEI Titan 80-300 electron microscope in STEM mode using the annular dark field (ADF) detector. Both probe convergence angle and the inner detection angle on the ADF detector was set to 18 mrad. The use of low inner detection angle maximizes the diffraction contrast that helps to distinguish individual grains in the deposited films. Compositional analysis was performed with a JEOL-ARM200F S/TEM operated at 200 kV. The energy dispersive x-ray spectroscopy (EDX) analysis was performed with a JEOL Centurio high-collection angle silicon drift detector (100 mm^2).The average columnar grain size of as-deposited and annealed thin films was measured from their respective plan view STEM images and using the linear intercept method. The distribution of Mg in the Al-Mg alloy films was determined using APT analysis of the thin films deposited on doped Si microtip arrays. The thin film coated Si microtips were subjected to annular milling to obtain needle specimens with specimen apex diameters less than 100nm. APT experiments were conducted using CAMECA LEAP 4000 XHR system in laser mode of evaporation using a 355nm wavelength pulsed UV laser at 20pJ laser pulse energy while specimen temperature was maintained at 40K and evaporation rate was maintained at 0.005 atoms per pulse. The APT results were reconstructed using Interactive Visualization and Analysis software (IVAS 3.6.12). For calculation of interfacial excess of solutes at the grain boundaries, cylindrical region of interest were extracted across grain boundaries and their Pos files were exported using IVAS software. The Pos files were read in to a custom Matlab script provided by X. Zhou et. al [53] from University of Alabama and is based on estimation of Gibbsian interfacial excess of solutes at grain boundaries by B. W. Krakauer et. al [54].Cross-section STEM samples were extracted from flat portions of the coated APT doped Si-microtip arrays by lift-out process using an FEI Dual beam focused ion beam-scanning electron microscope equipped with an omniprobe nanomanipulator and Pt-gas injection system.

3. Predicting Thermodynamically Preferred Nanocrystalline States in the Al-Mg System

The presence of a high volume fraction of grain boundaries in nanocrystalline materials has a significant impact on equilibrium solute distributions and thermodynamically preferred states relative to coarse-grained materials. Often, these features open up new opportunities for transforming properties via collective tuning of structure and chemistry that are not captured in classical alloy phase diagrams. To quantify the role of grain boundaries on solute distributions in nanocrystalline Al-Mg alloys, hybrid MC/MD simulations were performed to minimize system energy with respect to both solute configuration and local structural relaxations. Two average alloy compositions – 5 and 10 at.% Mg – were evolved at temperatures of 25 and 300 ^{o}C from the same initial nanocrystalline structure. The system energy drop and corresponding GB solute excess are shown in Fig. 1a for evolution at 25 ^{o}C. Partitioning of solute to the GBs drove the reduction in system energy, which was exacerbated in Al-10% Mg despite an identical solute excess in the grain boundaries. Atom maps are shown at 1.5 and 7.5 ns in Fig. 1b and 1c, respectively, with FCC atoms colored blue, HCP coordinated atoms (i.e. in stacking faults) dark blue, GB atoms grey, and Mg atoms red regardless of their location in the grain structure. After 1.5 ns, the structures evolved to contain heterogeneous solute distributions with greater Mg solute in the GBs relative to the interior of the grains, which persisted over the entire simulation and produced thermodynamically preferred solute stabilized nanocrystalline states for both alloy compositions.

Evolving the Al-Mg alloys at the higher temperature of 300 ^{o}C had a significant impact on the final state of the system as reflected in Fig. 1d by the emergence of two discrete energy drops. The initial reduction in system energy was attributed to the sharp increase in the GB solute excess and akin to the evolution at 25 ^{o}C. However, small subsets of atoms in the GBs of Fig. 1e exhibited icosahedral coordination after 1.5 ns at 300 ^{o}C captured by the yellow atoms and indicative of a new phase nucleating in the GBs, which is often referred to as a GB complexion [55, 56]. Further evolution of the system produced a second energy drop that was more pronounced for Al-10% Mg and accompanied by a sharp reduction in the GB solute excess. The icosahedral GB phase evolved into an ordered compound shown in the atom map after 7.5 ns in Fig. 1f with a composition of Al_2Mg (33.3 at.% Mg). With the precipitated configuration representing the lowest energy state at 300 ^oC (i.e., at the modeled time scales and relative to the solute stabilized nanocrystalline state containing GB segregation), Mg atoms were drawn out of the solute-rich GBs during the formation of Al_2Mg, thus accounting for the reduction in the GB solute excess that accompanied the second drop in the system energy. Given that the phase-separated nanocrystalline state containing Al2Mg precipitates represented the lowest energy state at 300 oC, Al-5% Mg also exhibited formation of this ordered compound with convergence of the GB solute excess to the same value as Al-10% Mg from Fig. 1d. The more subtle drop in system energy resulting from the Monte Carlo process in Al-5% Mg was attributed to the lower amount of solute available in Al-5% Mg to form the ordered Al2Mg phase relative to Al-10% Mg.There are a few of nuances deriving from the hybrid MC/MD simulation technique that influence formation of the ordered precipitates. First, from the Al-Mg phase diagram [26], the intermetallic compound that forms for Al-rich configurations is Al_3Mg_2 (37.5 at.% Mg), which has been reported with the complex β-Samson crystal structure that contains atomic clusters with coordination shells exhibiting icosahedral symmetry [57]. While icosahedral coordination was observed for the Al_2Mg compound in our simulations, the stoichiometry differed from the equilibrium intermetallic compound from the phase diagram and particularly contained less Mg. This disparity was attributed to the EAM potential, which was derived for dilute alloys of Mg in Al and not specifically optimized for the intermetallic Al_3Mg_2 phase [48]. Second, the thermodynamic driving force for formation of the ordered compound is actually greater at the lower evolution temperature of 25 ^oC. Its preferred formation at 300 ^oC was due to enhanced acceptance probabilities intrinsic to the Monte Carlo sampling method at elevated temperatures [47], which allows for more rapid evolution of the solute configuration. This is also promoted by increased atomic mobilities at elevated temperatures as previously noted during precipitation events in superalloys [58]. The disparate stoichiometry and anomalous temperature dependence notwithstanding, the tendency for precipitation and accompanying loss of solute from grain boundaries will lower the propensity for stabilization through GB segregation, but opens up new possibilities for enhancing thermal stability through Zener pinning [59]. The interplay of these two mechanisms are explored in the remaining sections with particular focus on correlating solute distributions and alloy stability in nanocrystalline Al-Mg thin films with the computational predictions of thermodynamically preferred nanocrystalline states.

4. Thermal Coarsening Resistance of Nanocrystalline Al-Mg Alloy Films

Thin films of Al-5% Mg and Al-10% Mg were sputter deposited for thermal stability measurements with nominally pure Al films also deposited to serve as a baseline. The plan view STEM images of pure Al, Al-5% Mg and Al-10% Mg alloy thin films are shown in Fig. 2. at the same magnification for both the as-sputtered and annealed conditions. Figs. 2(a-c) show that the average diameter of columnar grains of the sputtered pure Al, Al-5% Mg and Al-10% Mg films was 16.5 nm, 5.3 nm and 3.6 nm, respectively. The as-sputtered columnar grain diameter of Al-5% Mg is ~3x lower than that in pure Al and a further reduction of ~1.5x is observed when the Mg content increases to 10 at.%. Thus, the addition of Mg promoted the formation of a finer nanocrystalline grain structure during film deposition. Grain size reduction in a sputtered Al-alloy relative to pure Al film has also been observed previously by Lance Barron [60], where for a 300 nm film thickness, a pure Al film exhibited a grain size (measured by AFM) of ~100 nm as compared to ~60 nm for a Al-0.5 at.% Cu film. Grain refinement due to the addition of solute saturated at 0.5 at.% Cu with little change at higher Cu concentrations up to 1.5 at. %. Similar behavior was observed in ternary systems of Al-Cu-X where X was Cr or Ti in concentrations up to 2 at.%.

Upon annealing, it is expected that the columnar grains will transform to equiaxed grains[61, 62]. After annealing the average grain size of the pure Al, Al-5% Mg and Al-10% Mg films was measured to be 33 nm, 9.9 nm and 6.1 nm, respectively, as shown in Figs. 2 (d-f). After annealing, the grain size of Al-5% Mg is ~3.3x lower than in pure Al while the grain size of annealed Al-10% Mg is ~1.6x lower than in Al-5% Mg. In other words, for a given heat-treatment condition (as-sputtered or annealed), the grain size decreases with increasing Mg. The relative decrease in grain diameter/size between various Mg concentration films are the same in both as-sputtered and in annealed conditions. The images in Figs. 2(a-f) also show that the grain size in annealed Al, Al-5% Mg and Al-10% Mg represent a grain growth of 100% , 87% and 69%, respectively, relative to their respective as-sputtered grain sizes. Thus, while the annealed grain size is larger than the as-sputtered grain size in all the films, the extent to which the microstructure coarsened decreased with increasing Mg concentration.

5. Nanoscale Distribution of Mg: Segregation vs. Precipitation

The through-thickness distribution of Mg in the as-sputtered films was analyzed by STEM-EDS. The cross-section specimens for this analysis were prepared from the Al-Mg films deposited on the flat regions of the Si microtip array. Figs. 3(a) show the cross-section STEM image of as-sputtered 100nm thick Al-5% Mg film. The grain morphology near the film surface (top of the image) appears columnar while near the film/substrate interface (bottom of the image), the grains are narrower or v-shaped. Figs. 3(b-e) show the EDS elemental maps of Al, Mg, O and Si in as-sputtered Al-5% Mg. EDS maps show a clear segregation of Mg and O on the free surface of the films and at the film-Si substrate interface. In these STEM/EDS results of as-sputtered Al-5% Mg films, we found no evidence for segregation of Mg solute along the columnar grain boundaries, or the formation of any Al-Mg precipitates in the film. The SAED patterns from the film also did not reveal any presence of Mg rich precipitates as shown subsequently in figure 7. The overlap of several columnar grains within the thickness of TEM sample can influence the interpretation of solute segregation or precipitation using STEM/EDS images and hence a more detailed characterization of as-sputtered Al-5% Mg was performed using APT and the resulting data is shown in Figs. 4 (a-d). Figs. 4(a) and (b) show the APT reconstruction with Al (blue) and Mg (pink), respectively, in the as-sputtered Al-5% Mg film. Figs. 4(c) and (d) shows a 2D compositional contour map of Mg and Al, respectively, in a 1 nm x 10 nm x 35 nm slice to identify the location of Mg solute segregation and grain boundaries. The color scale showing the highest and lowest concentration of Mg and Al is given below the respective images. From the Mg 2D map in Fig. 4(c), a grain boundary with pronounced segregation of Mg is identified, which is marked using a red arrow. Mg segregation up to a maximum 7 at % was observed along the grain boundary. The Al 2D compositional contour map in Fig. 4(d) shows a corresponding depletion of Al atoms in the same region.

Now turning our attention to the analysis of as-sputtered Al-10% Mg film, the STEM image and EDS maps of as-sputtered Al-10% Mg are shown in Figs. 5 (a-e). Similar to Al-5% Mg EDS mapping results, no evidence was obtained for clear Mg segregation to grain boundaries. However segregation of Mg and O to film top surface and Si substrate-film interface was observed for Al-10% Mg film also as shown in fig 5(c) and (d). One isolated dark contrast precipitate region was observed in the STEM image of Al-10% Mg film as shown in fig 6(a).

STEM-EDS mapping was unable to quantify the composition of the precipitate (to enable its identification), due to its size being much smaller than the TEM sample thickness and hence EDS signal from the precipitate overlapping with the signals from surrounding matrix. Hence to better understand the compositional partitioning of Mg in the Al-10% Mg film APT analysis was conducted. Figs. 6(b) and (c) show the APT reconstruction with Al (blue) and Mg (pink), respectively, in the as-sputtered Al-10% Mg film. A local region with apparent pronounced segregation of Mg was evident which is highlighted using a dotted oval in Fig. 6(c). To clearly visualize the regions with Mg segregation, an iso-concentration surface for 20 at % Mg was plotted as shown in Fig 6(d). The oval-shaped region with locally high Mg content is clearly delineated as a distinct region in the Mg 20 at % iso-composition surface plot. The columnar grain boundaries with increased Mg segregation are also visible in the image. A thin rectangular slice of the APT data, using a 1nm x 25nm x 70 nm region highlighted by dashed rectangle in Fig. 4(c), was utilized to probe the composition change in Mg and Al. The 2D compositional maps of Mg and Al in this rectangular region are shown in Figs. 4(e) and (f) respectively. The region with highest Mg concentration (Fig. 4(e)) has a composition very close to 40 at % Mg and 60 at % Al (Fig. 4(f)) indicating the formation of isolated equilibrium Al_3Mg_2 precipitates.

To additionally analyze the presence of Al_3Mg_2 type precipitates in the films, selected area electron diffraction (SAED) patterns were collected from both as-deposited Al-5% Mg, Al-10% Mg films as well as films after annealing at 300°C for 3 hours. Fig. 7(a-b) show the SAED for as-deposited Al-5% Mg and Al-10% Mg films, respectively. For both as-deposited compositions, we identified the presence of diffraction rings that correspond to FCC matrix, but we cannot identify any diffraction spots that could be associated with Al_3Mg_2. Fig 7 (c) and (d) show the diffraction pattern of 300°C-3 hr annealed Al-5% Mg and Al-10% Mg films respectively. In addition to FCC rings, a few diffraction spots can now be additionally identified (as indicated by red arrows) that possibly correspond to either oxides or Al_3Mg_2 precipitates. The presence of only a few extra diffraction spots nevertheless suggests that only a negligible volume fraction of oxides or Al_3Mg_2 precipitates are present, and that a majority of Mg is associated with either grain boundaries or in bulk FCC solid solution phase.

The measured concentration from APT data for Al-5Mg is Al-97.88 at%-1.68 at% Mg-0.13 at% O, 0.20 at% Ga, and Al10Mg is Al-88.92 at%, Mg-10.92 at%, O-0.096 at% O, Ga-0.037 at%. This deviation of APT measured Mg concentration from nominal STEM-EDS measured average Mg concentration in Al-5Mg film is attributed to the small fraction of grain boundary regions with Mg segregation captured in the APT data volume given in figure 4, biasing the average concentration of dataset closer to the bulk grain interior concentration which is depleted in Mg.

6. Implications of Solute Heterogeneities for Thermal Stability

Solute heterogeneities deriving from grain boundary segregation and intermetallic precipitation can be better visualized by plotting the Mg concentration from the simulations separately for the solute stabilized and phase separated nanocrystalline states shown in the isometric views for Al-10% Mg in Fig. 8(a) and (b), respectively. Grain boundary segregation was conspicuously evident in the solute stabilized nanocrystalline state, but nearly eliminated upon the formation of the ordered Al_2Mg precipitates in the phase separated nanocrystalline state. The concentration of Mg was mapped across prototypical grain boundaries as a function of distance between the centers of two adjacent grains and shown in Fig. 8(c) and (d) for the Al-5% Mg and Al-10% Mg structures, respectively. The stable nanocrystalline state produced from evolution at 25 °C is characterized by elevated grain boundary solute contents for both alloy compositions and consistent with the alignment of Mg atoms with grain boundaries in the isometric view shown in Fig. 8(a). Precipitation of the Al_2Mg phase during evolution at 300 °C markedly reduced the grain boundary Mg content in Fig. 8(b). The maximum Mg concentration in the solute stabilized nanocrystalline state was approximately 12 and 19 at.% in Al-5% Mg and Al-10% Mg, respectively, which dropped to approximately 2.5 at.% in both alloys upon precipitation of Al_2Mg at the grain boundaries.

The experimental APT results in Figs. 4 and 6 demonstrated that Mg enriched grain boundaries were present in the both alloy films in the as-sputtered state. Segregation of Mg was also observed along columnar grain boundaries of the Al-10% Mg film, as shown in the cross-sectional view of the APT reconstruction along z-axis in Fig. 9(a) and the corresponding 20 at % Mg iso-concentration surface in Fig. 9(b). The grain boundaries containing elevated concentrations of Mg atoms are highlighted by arrows and the Al_3Mg_2 precipitate is outlined via the dotted circle. The extent of Mg segregation to grain boundaries was quantified using one dimensional composition profiles calculated using a 5nm diameter cylindrical region of interest with a length of 10 nm aligned perpendicular to grain boundary regions in the APT reconstruction. Representative composition profiles for Al-5% Mg and Al-10% Mg films are provided in Fig. 9(c) and (d) respectively. From the composition profiles, maximum grain boundary Mg concentrations in Al-5% Mg and Al-10% Mg were estimated to be approximately 5.5 and 20 at %, which are approximately 2.5 times greater than the solute concentration in the interior of grains.

The as-sputtered Al-5% Mg was observed to have an average interfacial excess of Mg between 1.56 to 3.18 atoms/nm2, which was enhanced in the as-sputtered Al-10% Mg and exhibited values between 4.26 and 14.33 atoms/nm2. From the simulations, the Mg GB excess for as-deposited Al5Mg was observed to be 25 atoms/nm2 for solute stabilized nanocrystalline state and about 6 atoms/nm2 in the case of phase separated state (Figure 1). The experimentally observed values of Mg GB excess for Al-5Mg are lower than these simulation predicted values indicating a low extent of solute enrichment at grain boundaries. In the case of Al-10 Mg alloy, the simulations predicted 25 atoms/nm2 for solute stabilized nanocrystalline state and about 6 atoms/nm2 for phase separated state (Figure 1). The experimentally measured Mg GB excess of Al-10Mg between 14.33 to 4.26 atoms/nm2 indicate that the Al-10Mg film has a combination of solute stabilized nanostructure and phase separated microstructure.

The experimentally measured grain boundary Mg concentration in Fig. 9(c) was less than the predicted values from simulations for Al-5% Mg from Fig. 8(c), but fell within the predicted range for the solute stabilized and phase separated nanocrystalline states. Conversely, the experimentally measured concentration of Mg in the grain boundaries of the as-sputtered Al-10% Mg was consistent with the grain boundary Mg concentration calculated for the solute stabilized nanocrystalline state from Fig. 8(d). Given that the formation of Al_3Mg_2 precipitates in the as-sputtered films occurred at only discrete locations (i.e. precipitates were not distributed uniformly throughout the microstructure), their influence on grain boundary segregation will be a more localized effect that depends on the proximity of the analyzed grain boundary to a precipitate. Thus, the lower grain boundary Mg concentration in the Al-5% Mg film was attributed to the formation of a low volume fraction of isolated nanoscale Al_3Mg_2 precipitates, consistent with Al_2Mg precipitation reducing the grain boundary solute excess in the phase separated nanocrystalline state from computational predictions.

The plan view TEM images of the Al and Al-Mg films in Fig. 2 showed that for identical heat-treatment conditions (i.e., 300 °C for 3 hours), the alloys exhibited less extensive grain growth than the pure Al film. Thus, not only did the addition of Mg inhibit grain coarsening, its ability to stabilize the nanostructure scaled with the Mg content. These observations are consistent with thermodynamic stabilization of nanocrystalline metals through grain boundary segregation reducing the grain boundary energy and hence the driving force for grain growth [63-65], which has been noted in other work on Al-Mg alloys [21]. However, our results also provide insights into the onset of instabilities due to intermetallic precipitation and its implications for sampling other mechanisms that can contribute to thermal stability. The simulations and experiments both confirmed the propensity for the Al-Mg system to form ordered intermetallic precipitates despite a high volume fraction of grain boundaries being available to accommodate solute atoms. In fact, grain boundaries were preferred sites for the formation of the precipitates due to their higher Mg concentration relative to the grain interiors. The equilibrium volume fraction of Al_3Mg_2 precipitates can be estimated using the phase diagram and our TEM and APT results. While the equilibrium solubility of Mg in Al at room-temperature is less than 1 at.%., sputtering at room temperature is a highly non-equilibrium process that enabled the production of films with 5 and 10 at.% Mg nominally in solid solution though we note the presence of few nanoscale Al_3Mg_2 precipitates from the TEM and APT analysis (Figs. 3-5). The formation of these precipitates in the as-sputtered films can be attributed to Mg diffusion along grain boundaries that produces local Mg enrichment and in turn, regions that exceeded the terminal solubility (~20 at.%).

Annealing at 300 °C is above the solvus of Al-5% Mg (~250 °C) and slightly below the solvus of Al-10% Mg (~330 °C). Under equilibrium conditions at 300 °C, 100% and 94% of Mg should be in solution in Al-5% Mg and Al-10 Mg, respectively. Upon cooling to room-temperature, the equilibrium volume fraction (by lever-rule) of Al_3Mg_2 in Al-5% Mg and Al-10% Mg should be ~10% and ~23%, respectively. The TEM diffraction pattern in Fig. 7 and APT results (Figs. 4, 6), both indicated that only a small number density of Al_3Mg_2 precipitates was present in both the as-deposited alloy films, i.e. the precipitate volume fraction was less than that predicted by the lever rule. APT results also demonstrated solute enrichment of the grain boundaries despite the presence of the Al_3Mg_2 precipitates. Collectively, grain boundary segregation and the reduced volume fraction of precipitates relative to equilibrium predictions from the phase diagram indicate the alloys occupied an intermediate state between the fully solute stabilized and phase separated states predicted from simulations. We thus attribute the enhanced thermal stability of the sputter deposited Al-Mg films to grain boundary segregation suppressing the driving force for coarsening coupled with nanoscale precipitates reducing the grain boundary mobility via a Zener pinning mechanism [66].

"Two additional extraneous effects are reported to influence grain boundary mobility and hence, grain size stabilization and grain growth. These include 1) influence of impurities in the sputter-deposited films and 2) the influence of film thickness on inhibiting grain growth during annealing through grain boundary grooving. Mo-Rigen He et al. showed that nominal concentration of 0.7 to 2.1 at% O in nanocrystalline Al lead to O segregation to grain boundaries, which in turn helped to enhance the critical stress for onset of grain boundary migration [67]. The measured average O concentration in Al-5Mg and Al-10Mg alloys in this work are far lower (below 0.2 at%) in comparison and hence we believe that O impurities do not play a significant role in restricting grain growth; instead, Mg segregation and intermetallic precipitation dominated thermal stability of the alloys relative to the pure Al film. During heat treatment, grain boundary grooving can occur in thin films that constrains grain growth, especially as the grain size approaches thin film thickness [68, 69]. The maximum grain size observed in this study even after annealing was 33 nm and still much smaller than the overall 100 nm thickness of the film. Furthermore, no conspicuous evidence of large-scale grain boundary grooving as reported in literature [68] was detected in the films studied here.. However, even if grain boundary grooving influenced stability of the films, it would be consistent across all three films (Al, Al-5Mg and Al-10Mg) due to their comparable thicknesses, thus allowing for a direct comparison of the behavior across the materials.

The results of this study demonstrate that deliberate selection of specific solute additions (e.g. Mg to Al in the current work) can enable simultaneous grain boundary segregation and intermetallic precipitation where nanoscale precipitates preferentially form at the grain boundaries due to their elevated solute concentration relative to the interior regions of the grains. Nanostructure stabilization will thus be governed by the combination of thermodynamic driving forces and kinetic barriers to grain coarsening. Complementary mechanisms that provide multiple pathways to achieve thermal stability through solute segregation and precipitation can expand the alloy selection parametric space beyond solvent-solute combinations that fit within either thermodynamic or kinetic stabilization criteria. We also note that the minimal degree of precipitate coarsening in the time scales studied in this work also demonstrates the potential of using this approach for designing alloys that can provide superior higher temperature properties through coarsening resistant precipitates.

7. Conclusion

In this study, we show that heterogeneous distributions of Mg in nanocrystalline Al-Mg alloys predicted by simulations and experimentally observed through APT plays a critical role in suppressing grain growth. In conjunction with a thermodynamic contribution due to grain boundary segregation, there is also a concurrent kinetic barrier due to the formation of nanoscale intermetallic precipitates identified in both the computational predictions and experimental results. The experimentally observed Mg concentration at grain boundaries in both Al-5% and Al-10% Mg films lies either at the computationally predicted Mg concentration at grain boundaries for solute-stabilized nanocrystalline Al-Mg, or in between this thermodynamically preferred state and a phase separated nanocrystalline state containing intermetallic precipitates that form preferentially at grain boundaries. This in turn implies concurrent occurrence of increased Mg segregation at Al-Mg grain boundaries and formation of a low volume fraction of Al_3Mg_2 precipitates. Hence, the coarsening resistance of nanocrystalline Al-Mg alloys upon heating was attributed to a synergistic effect involving Mg segregation to grain boundaries reducing the driving force for grain growth (i.e. thermodynamic contribution) and the formation of nanoscale Al_3Mg_2 precipitates pinning the boundaries against migration (kinetic contribution). Deliberate design of nanocrystalline alloys to exploit complementary stabilization mechanisms thus provides an opportunity for engineering coarsening resistant lightweight alloys in the Al, Mg and Ti systems.

Acknowledgements

This work was funded as a part of a laboratory directed research and development project under material synthesis and simulations across length scales (MS3) initiative in Pacific Northwest National Laboratory. AD would like to acknowledge Xuyang Zhou and Dr. Greg Thompson for graciously providing the matlab script to estimate the grain boundary excess of solute atoms from IVAS generated data. The sputter deposition, SEM, FIB, TEM and APT experiments were conducted at Environmental Molecular Sciences Laboratory, a DOE National user facility funded by office Biological and Environmental Research (DOE BER). WW and JRT acknowledge support from the National Science Foundation through Grant 1554411 and would like to thank Stony Brook Research Computing and Cyberinfrastructure, and the Institute for Advanced Computational Science, for access to the high-performance SeaWulf computing system, which was made possible by National Science Foundation Grant 1531492.

Figure captions

Figure 1: a) System energy drop and corresponding GB solute excess as a function of simulation time during evolution at 25 ^{o}C for Al-5% Mg and Al-10% Mg. The plateau in solute excess drove stabilization of the system energy with solute partitioned to the GBs in the snapshots at (b) 1.5 and (c) 7.5 ns, thereby producing a solute stabilized nanocrystalline state. Results are shown in (d) for evolution at 300 ^{o}C, and the initial energy drop due to GB segregation after 1.5 ns in (e) rapidly succumbed to the formation of Al_2Mg precipitates after 7.5 ns in (f), which manifested as a sharp decline in the GB solute excess and evolution of the system to a phase separated nanocrystalline state. The images shown in (b), (c), (e), (f) are 31.5x31.5 nm. The reader is referred to the web version of this article for interpretation of references to color.

Figure 2: STEM images of as-sputtered films of (a) pure Al (b) Al-5% Mg and (c) Al-10% Mg, deposited on the silicon nitride TEM windows; and STEM images of annealed (300C for 3 hours) films of (d) pure Al (e) Al-5% Mg and (f) Al-10% Mg.

Figure 3: a) Cross-sectional STEM image of as-sputtered Al-5% Mg thin film. STEM-EDS maps of Al-5% Mg showing distribution of (b) Al (c) Mg (d) O (e) Si.

Figure 4: APT results of as-sputtered Al-5% Mg showing distribution of (a) Al (blue) and (b) Mg (pink) atoms. 2D concentration map of (c) Mg and (d) Al with corresponding color map showing the observed variation in Mg and Al concentration along a grain boundary region. The location of grain boundary is indicated by red arrow.

Figure 5. a) Cross-sectional STEM image of Al-10% Mg thin film. STEM-EDS maps of Al-10% Mg showing distribution of (b) Al (c) Mg (d) O (e) Si.

Figure 6. (a) Cross sectional STEM image showing location of an isolated Mg rich precipitate in the film. APT results of as-sputtered Al-10% Mg film showing distribution of b) Al (blue) c) Mg (pink) with dotted oval shape highlighting the presence of a high Mg concentration region and dashed rectangle showing the area used for 2D compositional mapping. d) 20 at % Mg iso-concentration surface indicating the locations of high Mg concentration e) Mg 2D concentration map and f) Al 2D concentration map plotted using a 25nm x 1 nm x 70 nm slice of APT data with corresponding compositional scale shown below.

Figure 7: Diffraction pattern of as-sputtered (a)Al-5% Mg and (b)Al-10% Mg films, and after annealing (300 °C-3 hours) of (c) Al-5% Mg and (d) Al-10% Mg. white arrows in (a, c) index the rings from the matrix while the red arrows (c, d) indicate additional reflections possibly from Al_3Mg_2 precipitates.

Figure 8: Computationally predicted Mg atom distribution in (a) solute stabilized nanocrystalline and b) phase separated nanocrystalline Al-10% Mg alloys. Comparison of the predicted Mg concentration profiles across representative grain boundaries in c) Al-5% Mg and d) Al-10% Mg from the solute stabilized and phase separated nanocrystalline states.

Figure 9: The top-down view of APT reconstruction along z-axis showing (a) Mg distribution and (b) Mg 20 at % iso-concentration surface, with arrows indicating grain boundary as evidenced by the segregation of Mg atoms. Experimentally measured Mg concentration profile perpendicular to representative grain boundaries in as-sputtered c) Al-5% Mg and d) Al-10% Mg measured using APT.

References

[1] R.A. Andrievski, Review of thermal stability of nanomaterials, J Mater Sci 49(4) (2014) 1449-1460.
[2] M.A. Meyers, A. Mishra, D.J. Benson, Mechanical properties of nanocrystalline materials, Prog Mater Sci 51(4) (2006) 427-556.
[3] K.S. Kumar, H. Van Swygenhoven, S. Suresh, Mechanical behavior of nanocrystalline metals and alloys, Acta Materialia 51(19) (2003) 5743-5774.
[4] J.R. Trelewicz, C.A. Schuh, Grain boundary segregation and thermodynamically stable binary nanocrystalline alloys, Physical Review B 79(9) (2009).
[5] F. Liu, R. Kirchheim, Comparison between kinetic and thermodynamic effects on grain growth, Thin Solid Films 466(1-2) (2004) 108-113.
[6] F. Abdeljawad, S.M. Foiles, Stabilization of nanocrystalline alloys via grain boundary segregation: A diffuse interface model, Acta Materialia 101 (2015) 159-171.
[7] T. Chookajorn, H.A. Murdoch, C.A. Schuh, Design of Stable Nanocrystalline Alloys, Science 337(6097) (2012) 951-954.
[8] C.J. Marvel, D. Yin, P.R. Cantwell, M.P. Harmer, The influence of oxygen contamination on the thermal stability and hardness of nanocrystalline Ni–W alloys, Materials Science and Engineering: A 664 (2016) 49-57.
[9] C.J. Marvel, P.R. Cantwell, M.P. Harmer, The critical influence of carbon on the thermal stability of nanocrystalline Ni–W alloys, Scripta Materialia 96 (2015) 45-48.
[10] M. Saber, C.C. Koch, R.O. Scattergood, Thermodynamic Grain Size Stabilization Models: An Overview, Materials Research Letters 3(2) (2015) 65-75.
[11] W. Xu, L. Li, M. Saber, C.C. Koch, Y. Zhu, R.O. Scattergood, Microstructures and Stabilization Mechanisms of Nanocrystalline Iron-Chromium Alloys with Hafnium Addition, Metallurgical and Materials Transactions A 46(9) (2015) 4394-4404.
[12] K.A. Darling, B.K. VanLeeuwen, C.C. Koch, R.O. Scattergood, Thermal stability of nanocrystalline Fe–Zr alloys, Materials Science and Engineering: A 527(15) (2010) 3572-3580.
[13] H. Kotan, K.A. Darling, M. Saber, R.O. Scattergood, C.C. Koch, An in situ experimental study of grain growth in a nanocrystalline Fe91Ni8Zr1 alloy, J Mater Sci 48(5) (2013) 2251-2257.
[14] K.A. Darling, A.J. Roberts, Y. Mishin, S.N. Mathaudhu, L.J. Kecskes, Grain size stabilization of nanocrystalline copper at high temperatures by alloying with tantalum, J Alloy Compd 573 (2013) 142-150.
[15] B.C. Hornbuckle, T. Rojhirunsakool, M. Rajagopalan, T. Alam, G.P. Purja Pun, R. Banerjee, K.N. Solanki, Y. Mishin, L.J. Kecskes, K.A. Darling, Effect of Ta Solute Concentration on the Microstructural Evolution in Immiscible Cu-Ta Alloys, JOM 67(12) (2015) 2802-2809.

[16] D. Amram, C.A. Schuh, Interplay between thermodynamic and kinetic stabilization mechanisms in nanocrystalline Fe-Mg alloys, Acta Materialia 144 (2018) 447-458.
[17] M.A. Atwater, Darling, K.A, A Visual Library of Stability in Binary Metallic Systems: The Stabilization of Nanocrystalline Grain Size by Solute Addition: Part 1, 2012.
[18] C.C. Koch, I.A. Ovid'ko, S. Seal, S. Veprek, Structural Nanocrystalline Materials: Fundamentals and Applications, Cambridge University Press2007.
[19] Z. Pan, T.J. Rupert, Amorphous intergranular films as toughening structural features, Acta Materialia 89(0) (2015) 205-214.
[20] T. Frolov, M. Asta, Y. Mishin, Segregation-induced phase transformations in grain boundaries, Physical Review B 92(2) (2015) 020103.
[21] S.C. Pun, W. Wang, A. Khalajhedayati, J.D. Schuler, J.R. Trelewicz, T.J. Rupert, Nanocrystalline Al-Mg with extreme strength due to grain boundary doping, Materials Science and Engineering: A 696 (2017) 400-406.
[22] V.I. Razumovskiy, A.V. Ruban, I.M. Razumovskii, A.Y. Lozovoi, V.N. Butrim, Y.K. Vekilov, The effect of alloying elements on grain boundary and bulk cohesion in aluminum alloys: An ab initio study, Scripta Materialia 65(10) (2011) 926-929.
[23] X.Y. Liu, J.B. Adams, Grain-boundary segregation in Al–10%Mg alloys at hot working temperatures, Acta Materialia 46(10) (1998) 3467-3476.
[24] D.C. Paine, G.C. Weatherly, K.T. Aust, A STEM study of grain-boundary segregation in Al-6.5 wt% Mg alloy, J Mater Sci 21(12) (1986) 4257-4261.
[25] T. Malis, M.C. Chaturvedi, Grain-boundary segregation in an Al-8 wt % Mg alloy, J Mater Sci 17(5) (1982) 1479-1486.
[26] J.L. Murray, The Al-Mg (Aluminum-Magnesium) System, Bull. Alloy Phase Diagrams 3 (1982) 60-74.
[27] Y.S. Park, K.H. Chung, N.J. Kim, E.J. Lavernia, Microstructural investigation of nanocrystalline bulk Al-Mg alloy fabricated by cryomilling and extrusion, Materials Science and Engineering a-Structural Materials Properties Microstructure and Processing 374(1-2) (2004) 211-216.
[28] K.M. Youssef, R.O. Scattergood, K.L. Murty, C.C. Koch, Nanocrystalline Al-Mg alloy with ultrahigh strength and good ductility, Scripta Materialia 54(2) (2006) 251-256.
[29] F. Zhou, R. Rodriguez, E.J. Lavernia, Thermally stable nanocrystalline Al-Mg alloy powders produced by cryomilling, in: E. Ma, M. Atzmon, C.C. Koch (Eds.), Metastable, Mechanically Alloyed and Nanocrystalline Materials2002, pp. 409-414.
[30] B.B. Straumal, B. Baretzky, A.A. Mazilkin, F. Phillipp, O.A. Kogtenkova, M.N. Volkov, R.Z. Valiev, Formation of nanograined structure and decomposition of supersaturated solid solution during high pressure torsion of Al-Zn and Al-Mg alloys, Acta Materialia 52(15) (2004) 4469-4478.
[31] R. Hayes, V. Tellkamp, E. Lavernia, A preliminary creep study of a bulk nanocrystalline Al-Mg alloy, Scripta Materialia 41(7) (1999) 743-748.
[32] G.J. Fan, H. Choo, P.K. Liaw, E.J. Lavernia, Plastic deformation and fracture of ultrafine-grained Al-Mg alloys with a bimodal grain size distribution, Acta Materialia 54(7) (2006) 1759-1766.
[33] M.P. Liu, H.J. Roven, X.T. Liu, M. Murashkin, R.Z. Valiev, T. Ungar, L. Balogh, Grain refinement in nanostructured Al-Mg alloys subjected to high pressure torsion, J Mater Sci 45(17) (2010) 4659-4664.
[34] R. Goswami, P.S. Pao, S.B. Qadri, R.L. Holtz, Severe Plastic Deformation Induced Sensitization of Cryo-milled Nanocrystalline Al-7.5 Mg, Metallurgical and Materials Transactions a-Physical Metallurgy and Materials Science 45A(6) (2014) 2894-2898.
[35] F. Zhou, X.Z. Liao, Y.T. Zhu, S. Dallek, E.J. Lavernia, Microstructural evolution during recovery and recrystallization of a nanocrystalline Al-Mg alloy prepared by cryogenic ball milling, Acta Materialia 51(10) (2003) 2777-2791.

[36] M. Furukawa, Z. Horita, M. Nemoto, R.Z. Valiev, T.G. Langdon, Microhardness measurements and the Hall-Petch relationship in an Al-Mg alloy with submicrometer grain size, Acta Materialia 44(11) (1996) 4619-4629.
[37] B.Q. Han, F.A. Mohamed, C.C. Bampton, E.J. Lavernia, Improvement of toughness and ductility of a cryomilled Al-Mg alloy via microstructural modification, Metallurgical and Materials Transactions a-Physical Metallurgy and Materials Science 36A(8) (2005) 2081-2091.
[38] Z. Horita, D.J. Smith, M. Furukawa, M. Nemoto, R.Z. Valiev, T.G. Langdon, An investigation of grain boundaries in submicrometer-grained Al-Mg solid solution alloys using high-resolution electron microscopy, Journal of Materials Research 11(8) (1996) 1880-1890.
[39] J. Wang, Y. Iwahashi, Z. Horita, M. Furukawa, M. Nemoto, R.Z. Valiev, T.G. Langdon, An investigation of microstructural stability in an AlMg alloy with submicrometer grain size, Acta Materialia 44(7) (1996) 2973-2982.
[40] X. Sauvage, A. Ganeev, Y. Ivanisenko, N. Enikeev, M. Murashkin, R. Valiev, Grain Boundary Segregation in UFG Alloys Processed by Severe Plastic Deformation, Advanced Engineering Materials 14(11) (2012) 968-974.
[41] R.Z. Valiev, M.Y. Murashkin, A.V. Ganeev, N.A. Enikeev, Superstrength of nanostructured metals and alloys produced by severe plastic deformation, The Physics of Metals and Metallography 113(13) (2012) 1193-1201.
[42] I.A. Ovid'ko, A.G. Sheinerman, R.Z. Valiev, Mg segregations at and near deformation-distorted grain boundaries in ultrafine-grained Al–Mg alloys, J Mater Sci 49(19) (2014) 6682-6688.
[43] R.Z. Valiev, N.A. Enikeev, M.Y. Murashkin, V.U. Kazykhanov, X. Sauvage, On the origin of the extremely high strength of ultrafine-grained Al alloys produced by severe plastic deformation, Scripta Materialia 63(9) (2010) 949-952.
[44] X. Sauvage, N. Enikeev, R. Valiev, Y. Nasedkina, M. Murashkin, Atomic-scale analysis of the segregation and precipitation mechanisms in a severely deformed Al–Mg alloy, Acta Materialia 72 (2014) 125-136.
[45] A. Haslam, S. Phillpot, D. Wolf, D. Moldovan, H. Gleiter, Mechanisms of grain growth in nanocrystalline fcc metals by molecular-dynamics simulation, Materials Science and Engineering: A 318(1) (2001) 293-312.
[46] A.G. Frøseth, H. Van Swygenhoven, P.M. Derlet, Developing realistic grain boundary networks for use in molecular dynamics simulations, Acta Materialia 53(18) (2005) 4847-4856.
[47] B. Sadigh, P. Erhart, A. Stukowski, A. Caro, E. Martinez, L. Zepeda-Ruiz, Scalable parallel Monte Carlo algorithm for atomistic simulations of precipitation in alloys, Physical Review B 85(18) (2012).
[48] M.I. Mendelev, M. Asta, M.J. Rahman, J.J. Hoyt, Development of interatomic potentials appropriate for simulation of solid-liquid interface properties in Al-Mg alloys, Philos Mag 89(34-36) (2009) 3269-3285.
[49] S. Plimpton, Fast Parallel Algorithms for Short-Range Molecular Dynamics, Journal of Computational Physics 117(1) (1995) 1-19.
[50] A. Stukowski, Visualization and analysis of atomistic simulation data with OVITO–the Open Visualization Tool, Modelling and Simulation in Materials Science and Engineering 18(1) (2009) 015012.
[51] A. Stukowski, Structure identification methods for atomistic simulations of crystalline materials, Modelling and Simulation in Materials Science and Engineering 20(4) (2012) 045021.
[52] A.P. Sutton, R.W. Balluffi, Interfaces in crystalline materials, Clarendon, Oxford, 1995.
[53] X. Zhou, T. Kaub, R.L. Martens, G.B. Thompson, Influence of Fe(Cr) miscibility on thin film grain size and stress, Thin Solid Films 612 (2016) 29-35.
[54] B.W. Krakauer, D.N. Seidman, Absolute atomic-scale measurements of the Gibbsian interfacial excess of solute at internal interfaces, Physical Review B 48(9) (1993) 6724-6727.

[55] P.R. Cantwell, M. Tang, S.J. Dillon, J. Luo, G.S. Rohrer, M.P. Harmer, Grain boundary complexions, Acta Materialia 62 (2014) 1-48.
[56] J.D. Schuler, T.J. Rupert, Materials selection rules for amorphous complexion formation in binary metallic alloys, Acta Materialia 140 (2017) 196-205.
[57] K. Nakayama, H. Tsuruta, Y. Koyama, Formation of giant atomic clusters in the beta-Samson (beta-Al3Mg2) phase of the Al-Mg alloy system, Acta Materialia 128 (2017) 249-257.
[58] S. Eric, D.B. Paul, Identifying early stage precipitation in large-scale atomistic simulations of superalloys, Model Simul Mater Sc 25(3) (2017) 035005.
[59] B.C. Hornbuckle, T. Rojhirunsakool, M. Rajagopalan, T. Alam, G.P.P. Pun, R. Banerjee, K.N. Solanki, Y. Mishin, L.J. Kecskes, K.A. Darling, Effect of Ta Solute Concentration on the Microstructural Evolution in Immiscible Cu-Ta Alloys, Jom 67(12) (2015) 2802-2809.
[60] L. Barron, High-reflectance, sputter-deposited aluminum alloy thin thin films for micro-electro-mechanical systems, Rochester Institute of Technology, 2005.
[61] J. Humphreys, G.S. Rohrer, A. Rollett, Chapter 1 - Introduction, in: J. Humphreys, G.S. Rohrer, A. Rollett (Eds.), Recrystallization and Related Annealing Phenomena (Third Edition), Elsevier, Oxford, 2017, pp. 1-11.
[62] J.S. Riano, A.M. Hodge, Exploring the microstructural evolution of Hf-Ti: From nanometallic multilayers to nanostructures, Scripta Materialia 142 (2018) 55-60.
[63] O.K. Donaldson, K. Hattar, T. Kaub, G.B. Thompson, J.R. Trelewicz, Solute stabilization of nanocrystalline tungsten against abnormal grain growth, Journal of Materials Research (2017) 1-13.
[64] B.G. Clark, K. Hattar, M.T. Marshall, T. Chookajorn, B.L. Boyce, C.A. Schuh, Thermal Stability Comparison of Nanocrystalline Fe-Based Binary Alloy Pairs, JOM 68(6) (2016) 1625-1633.
[65] F. Abdeljawad, P. Lu, N. Argibay, B.G. Clark, B.L. Boyce, S.M. Foiles, Grain boundary segregation in immiscible nanocrystalline alloys, Acta Materialia 126 (2017) 528-539.
[66] M. Rajagopalan, K. Darling, S. Turnage, R.K. Koju, B. Hornbuckle, Y. Mishin, K.N. Solanki, Microstructural evolution in a nanocrystalline Cu-Ta alloy: A combined in-situ TEM and atomistic study, Materials & Design 113 (2017) 178-185.
[67] M.-R. He, S.K. Samudrala, G. Kim, P.J. Felfer, A.J. Breen, J.M. Cairney, D.S. Gianola, Linking stress-driven microstructural evolution in nanocrystalline aluminium with grain boundary doping of oxygen, Nature Communications 7 (2016) 11225.
[68] R. Dannenberg, E.A. Stach, J.R. Groza, B.J. Dresser, In-situ TEM observations of abnormal grain growth, coarsening, and substrate de-wetting in nanocrystalline Ag thin films, Thin Solid Films 370(1) (2000) 54-62.
[69] W.W. Mullins, The effect of thermal grooving on grain boundary motion, Acta Metallurgica 6(6) (1958) 414-427.

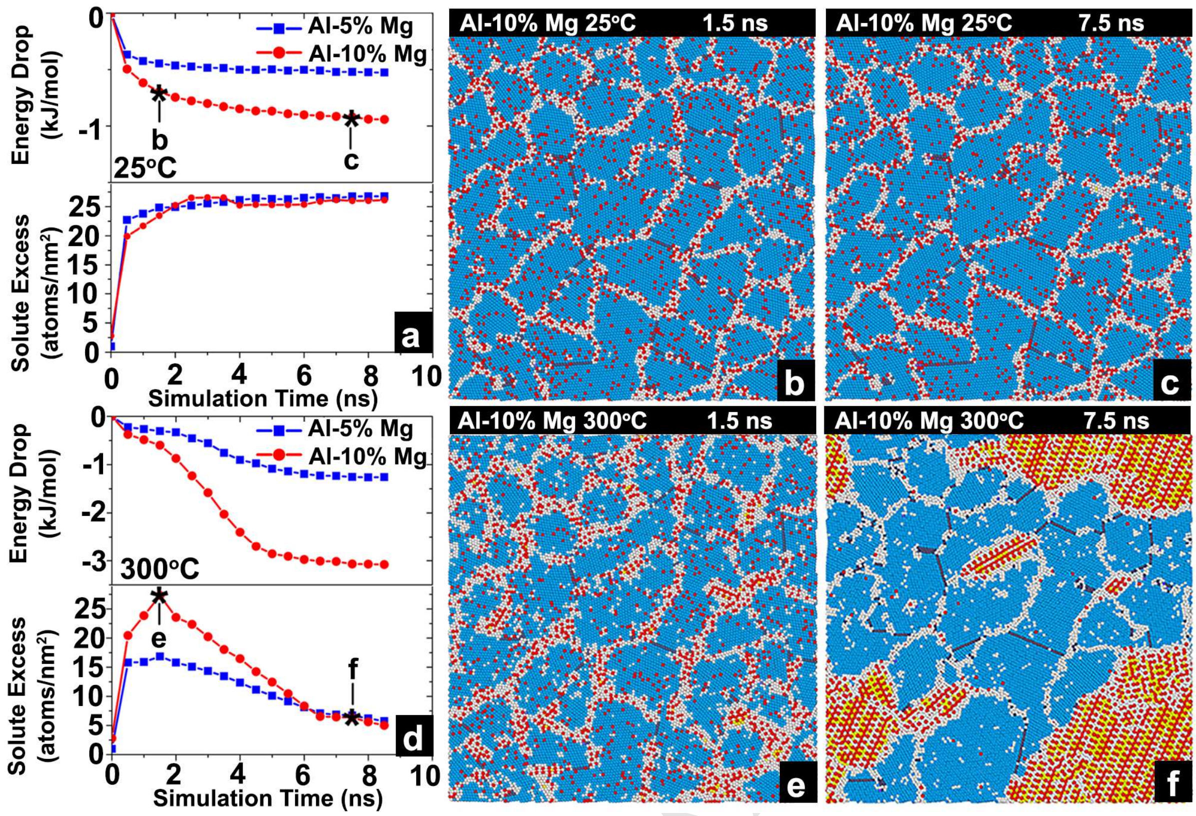

Energy Drop (kJ/mol)
Al-5% Mg
Al-10% Mg
b
c
25°C
Solute Excess (atoms/nm²)
a
Simulation Time (ns)
Al-10% Mg 25°C 1.5 ns
b
Al-10% Mg 25°C 7.5 ns
c
300°C
e
f
d
Al-10% Mg 300°C 1.5 ns
e
Al-10% Mg 300°C 7.5 ns
f

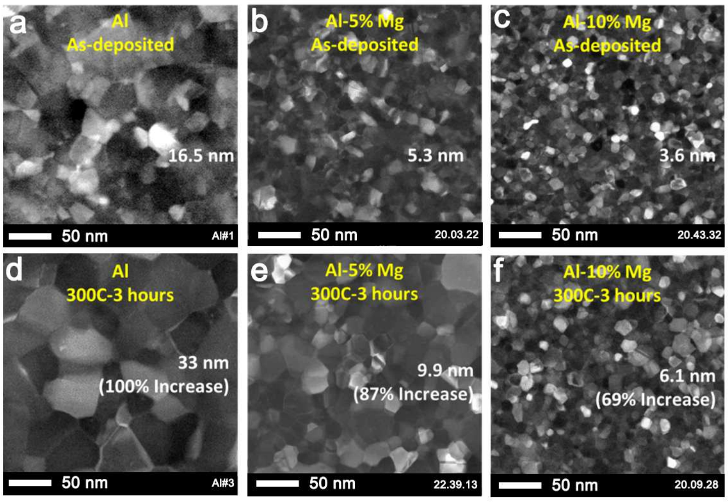

a
Al
As-deposited
16.5 nm
50 nm
Al#1
b
Al-5% Mg
As-deposited
5.3 nm
50 nm
20.03.22
c
Al-10% Mg
As-deposited
3.6 nm
50 nm
20.43.32
d
Al
300C-3 hours
33 nm
(100% Increase)
50 nm
Al#3
e
Al-5% Mg
300C-3 hours
9.9 nm
(87% Increase)
50 nm
22.39.13
f
Al-10% Mg
300C-3 hours
6.1 nm
(69% Increase)
50 nm
20.09.28

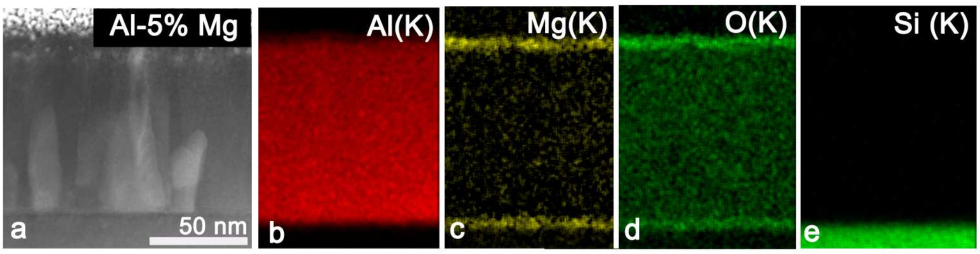
Al-5% Mg
a
50 nm
Al(K)
b
Mg(K)
c
O(K)
d
Si (K)
e

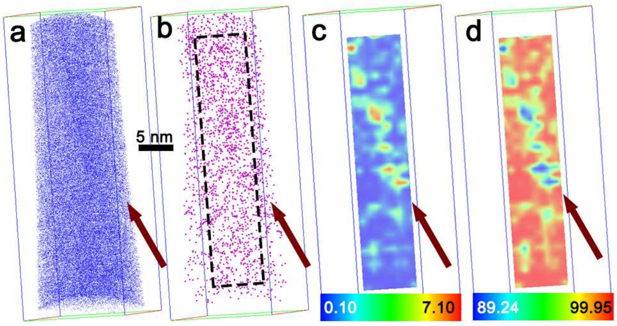
a
b
c
d
5 nm
0.10
7.10
89.24
99.95

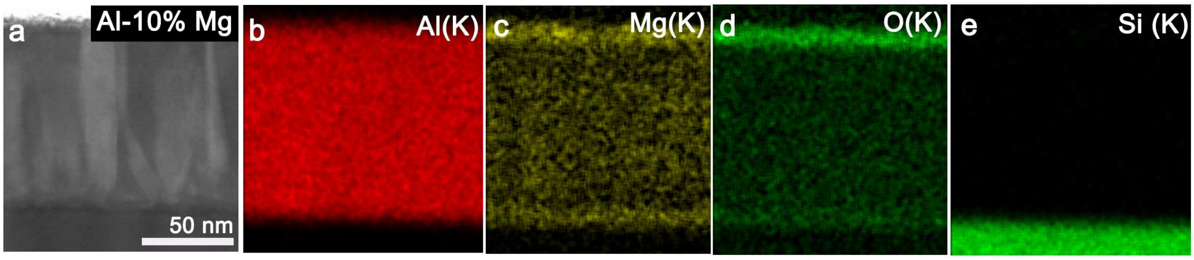
a
Al-10% Mg
50 nm
b
Al(K)
c
Mg(K)
d
O(K)
e
Si (K)

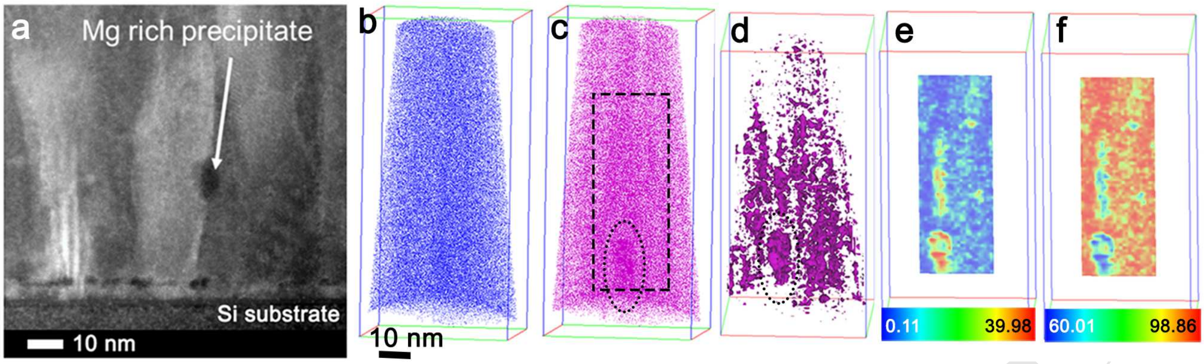
a
Mg rich precipitate
Si substrate
10 nm
b
c
d
e
f
10 nm
0.11
39.98
60.01
98.86

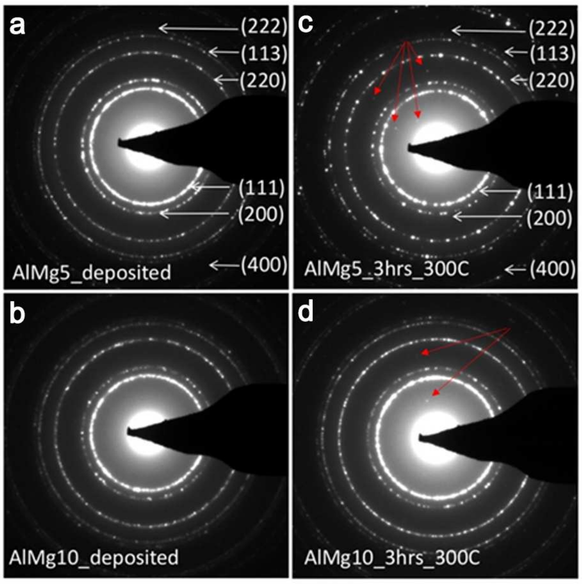
a
(222)
(113)
(220)
(111)
(200)
(400)
AlMg5_deposited
c
AlMg5_3hrs_300C
b
AlMg10_deposited
d
AlMg10_3hrs_300C

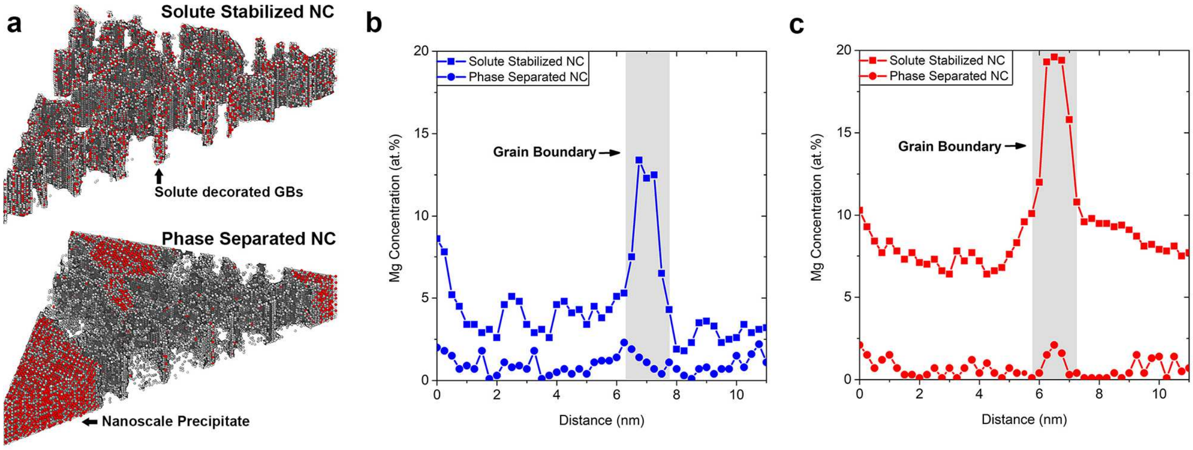
a
Solute Stabilized NC
Solute decorated GBs
Phase Separated NC
Nanoscale Precipitate
b
Solute Stabilized NC
Phase Separated NC
Grain Boundary
Mg Concentration (at.%)
Distance (nm)
c
Solute Stabilized NC
Phase Separated NC
Grain Boundary
Mg Concentration (at.%)
Distance (nm)

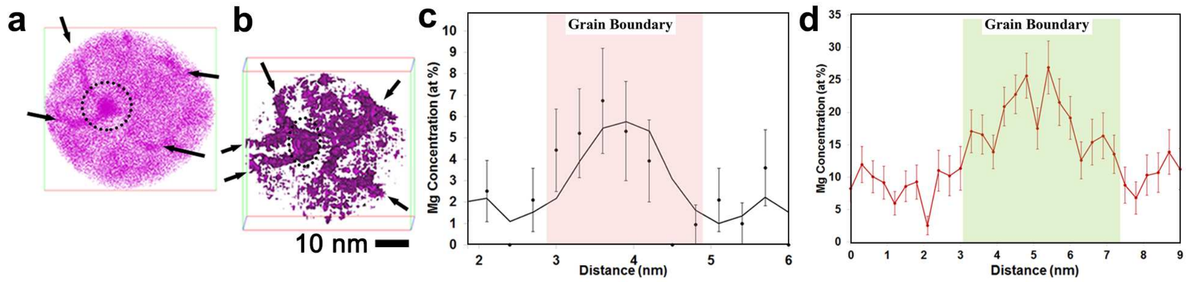
a
b
10 nm
c
Grain Boundary
Mg Concentration (at %)
Distance (nm)
d
Grain Boundary
Mg Concentration (at %)
Distance (nm)